https://doi.org/10.1016/j.msea.2020.140020
This is the Pre-Published Version.

Refractory alloying additions on the thermal stability and mechanical properties of high-entropy alloys

B.X. Cao[a], T. Yang[b], L. Fan [c], J.H. Luan [b], Z.B. Jiao [c], C.T. Liu [a, b,*]

[a] *Department of Materials Sciences and Engineering, City University of Hong Kong, Hong Kong, China*

[b] *Department of Mechanical Engineering, City University of Hong Kong, Hong Kong, China*

[c] *Department of Mechanical Engineering, The Hong Kong Polytechnic University, Hong Kong, China*

Abstract

In this study, alloying effects of Mo and W refractory elements on the microstructural evolution of high-entropy alloys (HEAs) were systematically studied. High-density $L1_2$-type precipitates formed during the isothermal treatment at 800℃. Alloying additions of Mo and W displayed different partitioning behaviors between the matrix and precipitate phases, with Mo partitioning to the matrix phase ($K_{Mo} = 0.45$) and W partitioning to the precipitates ($K_w = 0.95$) in the 1.5 at.% Mo and 1.5 at.% W alloyed HEA, respectively. A reversal in the partition of W back to the matrix ($K_w = 0.45$) was identified for the combined Mo and W alloying. It was demonstrated that W not only destabilized the Heusler phase at grain boundaries but also increased the volume fraction of the precipitates. In addition, lattice misfit was significantly reduced after alloying with these refractory additions. The coarsening kinetics was also quantitatively described according to the modified-Lifshitz-Slyozov-Wagner model. The coarsening rate constant for the HEAs was significantly reduced as comparison with that for Ni- and Co-based superalloys, implying an improved thermal stability of

© 2020. This manuscript version is made available under the CC-BY-NC-ND 4.0 license http://creativecommons.org/licenses/by-nc-nd/4.0/

HEAs. Moreover, a reduced interfacial energy together with inherently small diffusivity of the refractory elements attributed to the improved thermal stability. Our findings show the remarkable thermal stability for HEAs and the potential for HEAs to be developed as new high-temperature structural materials.

1. Introduction

Single-phased solid-solution high-entropy alloys (HEAs) have displayed an attractive combination of strength and ductility from cryogenic to ambient temperatures, but they became soft at elevated temperatures [1–5]. Potent strengthening mechanisms at ambient and cryogenic temperatures, such as grain boundary strengthening and strain hardening, are not effective at elevated temperatures. For example, the yield strength of a CoCrFeMnNi HEA was 562 MPa at -196℃ , but quickly dropped to only 148MPa at 800℃ [2]. Using a second phase for strengthening among HEAs provides an effective strategy for designing high-temperature structural materials, which breaks the long-standing concept to maintain a single solid-solution phase in HEAs [6–8]. The introduction of $L1_2$-type ordered intermetallic phase (γ') to the face-centered-cubic matrix (γ) in HEAs can effectively strengthen the materials without causing any embrittlement [9]. The fully coherent interface between the γ matrix and γ' precipitates reduces the nucleation barrier, resulting in the precipitation of high-density nano-sized $L1_2$-type precipitates. Since then, extensive efforts have been made to investigate $L1_2$-precipitate strengthened HEAs.

The characteristic matrix/precipitates microstructure resembles to that of

superalloys. Superalloys are developed to serve under high-stress and high-temperature environments, which have displayed the unusual high-temperature strength and thermal stability [10–12]. Conventional superalloys are also multicomponent alloys with possibly over ten alloying elements [13,14]; however, there are still dominated by one or two principal elements, such as Ni- and Co-based superalloys. In contrast, the compositions of HEAs lie in the center part of the phase diagrams containing multiple-principle elements. Recently the development of precipitation-hardened HEAs (PH-HEAs) has shown remarkable high-temperature properties [15–18], rendering them with a great potential for high-temperature structural applications.

Operations at higher temperatures are highly desired, which are driven by the demand from the energy efficiency considerations [19]. Conventional superalloys are frequently improved to meet the industrial demand for a higher operation temperature by modifying compositions and/or processes. The microstructures and compositions of both the matrix and precipitates are optimized towards this end. In the developing history of superalloys, refractory elements have been introduced since the beginning of superalloy development [20–22]. Refractory elements including Mo, W, and Re generally provide a high-temperature strength and creep resistance to superalloys by acting as potent solid-solution strengtheners in the ductile γ matrix phase. Among all the possible refractory elements, Re is the most effective one. It is demon- strated that 1.6 wt% Mo or W is required to replace 1 wt% Re in the γ matrix phase in order to achieve the same solid-solution hardening efficiency [23]. However, the Re content also brings up other issues, including poor oxidation resistance [24] and embrittlement caused by

the formation of brittle topologically close-packed (TCP) phases [25]. Moreover, as a unique strategic resource, the cost of Re alloying is extremely high [26]. As a result, the developments of Re-free superalloys become a research hotspot with the aim of reducing cost and achieving enhanced microstructural stability. To this end, Mo and W elements can be used to substitute for Re to provide solid-solution strengthening.

Apart from the benefit from the solid-solution strengthening effect, Mo additions can also increase the γ'-phase solvus temperature, resulting in increased the high-temperature strength and creep resistance in Ni-base superalloys [27]. The W element, a γ'-former element, partitioning into the γ' phase among Co-based superalloys, stabilizes the γ' phase [12]. However, the effect of Mo and W to the precipitate phase stability among PH-HEAs is still not clear at the present time. Moreover, it is expected that the growth kinetics of precipitates would be altered by alloying with refractory elements which generally influence the diffusivity of solute elements. Small diffusivity generally retards precipitate coarsening under long-time thermal treatments. The addition of 2 at.% tungsten to ternary Ni–Al–Cr alloys reduced the coarsening rate constant by 1/3 at 800℃ [22]. Mo additions also retard γ' coarsening at 925℃ [28]. Moreover, the synergistic effect of Mo and W additions has been observed by increasing the solubility of Mo in the phase to which W partitions among commercial superalloys [29]. The presence of the combined Mo and W elements in Ni–Cr–Al–Ti alloy reduced the diffu- sivities of both Ti and Cr at 900℃, and therefore influencing the particle coarsening [10]. However, the benefit of the synergistic Mo and W partitioning behavior and associated influence on solute diffusivity and coarsening behavior has not

been well studied at the present time.

This work systematically investigates the alloying effect of Mo and W on HEAs. The microstructural evolution, coarsening kinetics, grainboundary phase evolution, as well as the mechanical behavior were carefully investigated. Cutting-edge atomic-scale tools, such as atom probe tomography (APT), was used to study the elemental partitioning behavior. Modified Lifshitz-Slyozov-Wagner model was utilized to quantitatively describe the temporal evolution of the precipitates and their coarsening kinetics.

2. Experimental

2.1 Alloy design and preparation

Alloy design in this work based on the following considerations: (1) the concentrations of Ni and Co were controlled to be 30 at.% to stabilize the fcc matrix; (2) Cr content was tailored to be 15 at.% to avoid the formation of the σ phase [30]; (3) a small amount of Al and Ti additions (6 at.%), which act as strong γ'-former elements, was introduced into the NiCoFeCr-based high-entropy matrix, leading to the high-density $L1_2$-type precipitation for precipitation hardening. Thermodynamic calculations were conducted to obtain the phase diagrams and critical heat treatment temperatures via the Thermo-Calc Software in TTNI8 database. As shown in Fig. 1a, the γ solidus temperature and γ' solvus temperature are 1263℃ and 1116℃ for the $Ni_{30}Co_{30}Fe_{13}Cr_{15}Al_6Ti_6$ HEA, respectively. The γ' precipitation coexists well with the

γ matrix in the temperature range between 750℃ and 1116℃ in the $Ni_{30}Co_{30}Fe_{13}Cr_{15}Al_6Ti_6$ HEA without the formation of other intermetallic phases. The γ solidus temperature and γ' solvus temperature are slightly influenced by both Mo and W additions (see Fig. 1b). Therefore, $Ni_{30}Co_{30}Fe_{13}Cr_{15}Al_6Ti_6$ HEA is a suitable candidate for high-temperature structural applications, which was thereby selected as the prototype alloy in present work and to systematically analysis the γ' precipitation coarsening behaviour.

Alloys were prepared by arc-melting high-purity raw metals in a Tigetter Ar atmosphere. The HEA with a nominal composition of $Ni_{30}Co_{30}Fe_{13}Cr_{15}Al_6Ti_6$ (at.%) is denoted as the base HEA. The base HEA is further modified by alloying with 1.5 at.% refractory elements, with three different compositions: $(Ni_{30}Co_{30}Fe_{13}Cr_{15}Al_6Ti_6)_{98.5}Mo_{1.5}$ (Mo1.5 HEA), $(Ni_{30}Co_{30}Fe_{13}Cr_{15}Al_6Ti_6)_{98.5}W_{1.5}$ (W1.5 HEA), and $(Ni_{30}Co_{30}Fe_{13}Cr_{15}Al_6Ti_6)_{98.5}Mo_{0.6}W_{0.9}$ ((MoW)1.5 HEA). The ingots were flipped and remelted at least five times to ensure a chemical homogeneity, and then dropped into a copper mold with a size of $5\times12\times100mm^3$. The as-cast samples were homogenized at 1165℃ for 2h, followed by cold-rolling (~65% reduction in thickness) along the longitude direction. The heavily cool-rolled samples were treated at 1165℃ for 6 min for full recrystallization. Then the recrystallized HEAs were isothermally aged at 800℃ for 24, 72, 168, and 336 h for precipitation growth. All the heat treatments are conducted in air and followed by air cooling to room temperature.

2.2 Microstructural characterizations

Microstructural characterizations were carried out using scanning electron microscopy (SEM, Quanta 450 FEG), transmission electron microscopy (TEM, JEOL 2100F) and X-ray diffractometer (XRD, Rigaku). For the SEM observation, samples were first grounded me- chanically by SiC papers from 120 grit to 2500 grit, followed by elec- tropolishing using an electrolyte of 20 vol% nitric acid and 80 vol% ethanol at 20V and $-30℃$. For the TEM examination, specimens were first grounded to a thickness of 50 μm using SiC papers, then punched into discs with a diameter of 3 mm, followed by ion-milling to electron transparency via a precision ion polishing system (Ganta 695). For phase identification and lattice parameter calculations, the diffraction data were collected from 20° to 100° with a step size of 0.02° and a speed of 2° per minute. The (311) diffraction peaks of γ and γ' phases were deconvoluted for solving the individual lattice parameters of γ and γ' phases [9]. In order to distinguish the individual peak of the γ' phase and γ phase from the overlapped peak, a pseudo-Voigt function was used for a peak deconvolution.

Atomic-scale compositional analysis was carried out by Atom probe tomography (APT). APT is a state-of-art three-dimensional elemental analytical method with an atomic-scale resolution. As compared with traditional characterization method, its outstanding spatial resolution (~0.1 nm) and detection sensitivity (down to ppm-level concentration) make it possible for capturing atomic-scale phenomena such as solute segregation and cluster formation. Needle-shape specimens were fabri- cated and extracted using a FEI Scios dual-beam SEM/focused-ion-beam instrument. A cleaning

procedure of 2 kV and 27 pA in the final step was used to remove the contaminated surface caused by previous high- energy Ga ion beams. The APT test was conducted via a local elec- trode atom probe (CAMECA LEAP 5000 XR) in a voltage mode at 70 K with a pulse rate of 200 kHz, a pulse fraction of 20%, and a detection rate of 0.2%. Image Visualization and Analysis Software package (IVAS 3.8.2) was used for 3D reconstructions.

2.3 Mechanical properties

The temporal evolution of the microhardness was measured by a Vickers micro-hardness tester (Fischer HM2000XY) with a nominal load of 2 N and a dwell time of 15 s. The hardness value reported here was an average of at least 9 measurements.

Dog-bone-shaped specimens with a gauge length of 25 mm with a cross-section area of $2.5\times1.5mm^2$ were cut by electro-discharge machining for tensile tests. Surfaces of the specimen were polished to 2500 grit by SiC papers. The tensile test was conducted by a SUST CMT5304GL testing machine at 800℃ with a strain rate of $10^{-3}s^{-1}$ in air.During the high-temperature tensile test, all the specimens were heated in the furnace from room temperature to 800℃ under a preload of 50MPa. The temperature was monitored by three different thermocouples, maintaining temperature variation within ±5℃ during the hightemperature tensile tests. The yield strength at 800℃ was taken as an indicator for the high-temperature strength.

2.4. Coarsening parameters of γ' precipitates

The size of γ' precipitates was estimated according to the method of equivalent circle radius [31]. At least 200 precipitates were involved in determining the average size of precipitates for each sample. The average equivalent circle radius (r) was calculated according to the following equations:

$$r_p = \sqrt{A_p / \pi} \tag{1}$$

$$r = \frac{1}{n}\sum_{i=1}^{n} r_p^i \tag{2}$$

where A_p is the area of the precipitation, r_p is the equivalent circle radius of the precipitates, n is the total number of precipitates involved

The Ostwald ripening mechanism assumes that the large particle growth at the expense of dissolving small particles through a solute diffusion in the matrix phase. Basically, the driving force for precipitate coarsening is to decrease the interfacial energy between the matrix and precipitate. Lifshitz, Slyozov, and Wagner (LSW) had developed the classical numerical model for quantifying this kind of coarsening behaviour [32,33]. However, there are few assumptions in the LSW model that are not applicable to the situation we encountered in this work. In the original LSW model, it is assumed that the condensation of the solute atoms from a dilute matrix leads to the growing precipitates, where the interference from the diffusion fields of adjacent particles is neglected. In fact, a high volume fraction of the precipitates is main- tained in the present study, so the overlap among the diffusion fields between neighboring particles should be taken into consideration. As a result, several optimized LSW models

have been put forward in order to eliminate such discrepancy[34–37]. Collectively, a more generalized model can be used to evaluate the coarsening kinetics[20]:

$$r(t)^n - r(t_0)^n = K_r(t - t_0) \quad (3)$$

where $r^{(t)}$ and (rt_0) represent the average equivalent circle radius at time t and at the beginning of coarsening, K_r is coarsening rate constant, and n is the temporal exponent of precipitation size. Different from the original LSW model which yields a fix temporal exponent $n = 3$, the generalized model treats this parameter as a variable. For the case that $n = 2$, the coarsening process is controlled by the trans-interface diffusion[38], rather than bulk diffusion when $n = 3$ [39].

3 Results and discussion

3.1 Microstructures and elemental profiles at 800℃

Aging at 800℃ induced a uniformly distributed precipitation, where the size of precipitates gradually increased with the increase of aging time (Fig. 2 and Table 1). Precipitation morphology was further characterized by TEM. Dark-field TEM (Fig. 3a) showed a homogenous distribution of high-density cuboidal precipitates with rounded corners embedded in the matrix after aging for 336 h. Corresponding select area electron diffraction (SAED) patterns acquired from $z = [011]$ exhibited the superlattice diffraction spots, as pointed out by red circles, revealing the $L1_2$-type ordered structure of the precipitates.

Composition analyses towards the nano-size phase were carried out by TEM energy-dispersive X-ray spectroscopy (EDX) for HEAs after aging for 336 h at 800℃ (Table 2). Partitioning coefficient K_i (i Ni, Co, Fe, Cr, Al, Ti, Mo, W) are also listed to quantitatively illustrate elemental partitioning behavior which can be derived as:

$$K_i = C_i^{\gamma'} / C_i^{\gamma} \tag{4}$$

where $C_i^{\gamma'}$ and C_i^{γ} are the atomic percentage of element i in the γ' and γ phase, respectively. The values of K_i are listed in Table 2. Elemental partitioning coefficient $K_i > 1$ represents the element partitions to γ' precipitates, otherwise to the γ matrix. Similar to previous reported PH-HEAs [6,9,15], the γ' precipitates are enriched in Ni, Al, and Ti and depleted in Fe, Co, and Cr. The partitioning coefficient of Ni, Co, Fe, and Cr remains relatively stable after alloying with refractory elements. The partitioning coefficient of Al decreased significantly from 6.40 for the base HEA to 2.89 for Mo1.5 HEA, 3.22 for W1.5 HEA, and 2.55 for (MoW)1.5 HEA (Fig. 3c). As a result, Ti atoms partitioned more strongly to the precipitates and occupied the corner sites that are used to be filled wiht Al atoms in the base HEA, leading to the increased $K_{Ti.}$

Mo and W demonstrated a different partitioning behavior when alloyed separately: $K_{Mo} = 0.46$ and $K_W = 1.54$. Mo preferred to partition to the γ' precipitates (Table 2). The combined alloying effect of Mo and W is revealed in (MoW) 1.5 HEA with a norninal composition of 0.6 at.% Mo and 0.9 at.% W. Partitioning coefficient K_W decreased from 1.54 when alloyed solely to 0.92 when alloyed combined with Mo, suggesting W repartitioned to the γ matrix.

Equiaxial grain structure of the as-recrystallized samples was demonstrated in Fig. 4a. We did not identify any grain-boundary phase formation after recrystallization. In contrast, the Heusler phase formed at grain boundaries after aging at 800℃ (Fig. 4b). In terms of grain sizes, we observed almost negligible grain growth even after aging at 800 °C for 336 h (Fig. 5a). It is well known that the dispersed particles along grain boundary (GB) exert a pinning force on the GB migration, leading to the grain growth inhibition at this temperature [40]. In this case, either the high-density γ' precipitates in the grain interior or the Heusler phase located at the GBs balanced the driving force for the grain growth by a strong pinning effect.

The Heusler phase was identified at the grain-boundary region after a long-time aging (Fig. 4b), whose volume fraction was determined by image extraction using ImageJ software. The volume fraction of the Heusler phase was determined as 1.26% in the base HEA (Fig. 5b). Mo and W demonstrated different contributions to such grain-boundary Heusler phase. That is, alloying 1.5 at.% Mo increased the Heusler phase amount to 1.59%, whereas 1.5 at.% W decreased the amount of the Heusler phase to only 0.31%. The volume fraction of the Heusler phase in the (MoW)1.5 HEA was 0.74%, which was also lower than that of the base HEA. It is concluded that Mo contributes to a grain-boundary Heusler phase formation and W suppresses Heusler phase formation. As shown in the elemental mapping results (Fig. 5c), the Heusler phase was enriched with Al and Ti. The lattice constant of the Heusler phase was determined to be 0.6046nm from the diffraction patterns taken from $[1\bar{1}1]$ shown in the inset of Fig. 5c. The Heusler phase is extremely brittle and incoherent with the surrounded γ

matrix. The formation of the Heusler phase contributes to a localized stress concentration and results in an early brittle fracture under loading [6].

The volume fraction of $L1_2$-type precipitates was calculated according to lever rules. Due to the presence of the Heusler phase, the lever rule was modified by taking a consideration of the Heusler phase, into the mass balance equation:

$$\varphi^{\gamma'} C_{\gamma'} + \varphi^{\text{Heusler}} C_{\text{Heusler}} + \left(1 - \varphi^{\gamma'} - \varphi^{\text{Heusler}}\right) C_{\gamma} = C_m \tag{5}$$

where $\varphi^{\gamma'}$ and φ^{Heusler} are the volume fraction of the γ' phase and Heusler phase, respectively, $C_{\gamma'}$ and C_{γ} are the elemental concentration for γ' precipitates and the γ matrix , respectively, $C^{Heusler}$ is the concentration of elements in the Heusler phase, and C_m is the the bulk concentration of elements in the alloy. In this way , the volume fraction of the γ' phase can be derived from equation (6):

$$\varphi^{\gamma'} = \frac{C_{\text{m}} - C_{\gamma} - \varphi^{\text{Heusler}} \left(C_{\text{Heusler}} - C_{\gamma}\right)}{\text{C}_{\gamma'} - \text{C}_{\gamma}} \tag{6}$$

The value of $\varphi^{\gamma'}$ is calculated to be 38.8 ± 1.2% for the base HEA after aging for 336 h (Fig. 5d). It slightly decreased to 34.5 ± 0.9% after alloying with the 1.5 at.% Mo. Alloying with 1.5 at.% W increased $\varphi^{\gamma'}$ to ± 3.0% after aging for 336 h. For the (MoW)1.5 HEA, the value of $\varphi^{\gamma'}$ was determined as 36.5 3.4%. Because Mo does not contribute to the precipitation formation, it influences the partitioning behavior of other elements, leading to the varied $\varphi^{\gamma'}$ [41]. In contrast, W is regarded as a γ'-former element in Co-based superalloys, leading to Co_3(Al,W) precipitates. It is anticipated that the positive contribution to the pre- cipitation reaction through W alloying in the PH-HEAs.

3.2 Lattice misfit measurement

he lattice misfit between the precipitates and the matrix was evaluated by the deconvolution of XRD peaks. The experimental XRD peaks in the black color (see Fig. 6) for the (311) plane. Peak splitting phe- nomenon resulted from the difference in the lattice parameters of the γ' phase and γ phase. Peak splitting became less discernible after alloying with the refractory elements, especially for the (MoW)1.5 HEA. The deconvoluted γ' phase peak (yellow color) stood at a low angle as compared with the γ phase peak (green color), suggesting a larger lattice parameter for the γ' phase. Because of the larger atomic radius of Mo and W, it leads to the lattice expansion after the solid solution with these refractory elements. As shown in Fig. 7a, the lattice parameters of both the γ' phase and γ phase expanded after Mo or W alloyed. In addition, the γ' and γ phase lattice parameters of W1.5 HEA was larger than that of Mo1.5 HEA, which can be explained by the larger atomic size of W [42].

It should be noted that the lattice constant of the γ phase in (MoW)1.5 HEA was even larger than that of W1.5 HEA although a part of W atoms was replaced by Mo atoms. The reverse partitioning of W (Fig. 3c) from the γ′ phase to the γ phase in (MoW)1.5 HEA led to the lattice further expansion in the γ phase of (MoW)1.5 HEA. Both Mo and W atoms partitioned to the γ phase in (MoW)1.5 HEA, rendering the largest γ phase lattice parameter in (MoW)1.5 HEA.

The lattice misfit (δ) between the γ' and γ phases is defined as :

$$\delta = 2\left(a_{\gamma}' - a_{\gamma}\right) / \left(a_{\gamma'} + a_{\gamma}\right) \quad (7)$$

where $a_{\gamma'}$ and a_{γ} are the lattice constant for the γ' phase and phase separately.

All the four HEAs exhibited a positive lattice misfit after aging at 800℃ C for 336h at room temperature. The lattice misfit for the base HEA was 0.3549%. It is changed to 0.2702%, 0.3032%, and 0.2642% for Mo1.5 HEA, W1.5 HEA, and (MoW)1.5 HEA. The lattice misfit was the lowest for the (MoW)1.5 among all the four HEAs studied. Clearly, a carefully adjusted Mo/W ratio is important in tailoring the lattice misfit for the high-temperature alloy design. The coarsening behavior is closely related to the lattice misfit at different temperatures. The thermal expansion coefficient of the γ' phase is lower than that of the γ phase due to the long-range-ordered structure in γ' phase [43]. Because the thermal expansion of the lattice parameter in the γ phase is smaller than that of the γ phase, it leads to a decreased lattice misfit as the temperature increased. The lattice misfit of Ni-base superalloys is usually negative at room temperature. On the contrary, the lattice constant of the γ' phase in the current study was slighter larger than that of the γ phase, thus a positive lattice misfit was maintained. The lattice misfit becomes more negative and larger in magnitude with the increased temperature among some Ni-base superalloys with a negative lattice misfit [44], whereas the lattice misfit of current HEAs became smaller in magnitude at higher temperatures. Svoboda et al. [45] demonstrated that, for the optimal creep strength, the magnitude of lattice misfit should be larger at lower temperatures and smaller at higher temperatures. It is expected that the current alloys with a positive lattice misfit could demonstrate a better creep resistance [44].

3.3 Mechanical properties

The microhardness test provides a useful information for the precipitation hardening evolutions. An empirical relationship between hardness and yield strength has been generally accepted and widely used extensively: the hardness values is approximately three times the value of yield strength [46,47]. It should be noted that it is only appli- cable to materials without much work hardenability. For work-hardening metals, the yield strength should be replaced by the flow strength at a strain value between 8% and 10% (for Vickers indentation) since work hardening can be introduced during indentation[48]. Fig. 8a displayed the microhardness evolution as a function of aging time. The microhardness value for the samples without aging refers to the microhardness of recrystallized specimens. Since the specimens were air-cooled from the recrystallization temperature (1165℃) to room temperature, precipitation formed during the cooling process[15]. As a result, the microhardness value of the air-cooled specimens cannot be regarded as the hardness of the γ matrix phase due to the rapid nucleation and precipitation process. Dramatic microhardness increment can be found after aging for 24h (Table 3). All the four HEAs reached a peak hardness after 168h aging with a hardness of 451 8 HV for the base HEA, 454±13 HV for the Mo1.5 HEA, 463±8 HV for the W1.5 HEA, and 465±14 HV for (MoW)1.5 HEA. An extended aging time led to the microhardness decrement after 168 h, as indicated in Fig. 8a.

High-temperature strength is critical in evaluating the potential of PH-HEAs for high-temperature applications. The yield strength at 800℃ is shown in Fig. 8b. Refractory elements alloyed PH-HEAs exhibited an enhanced strength at 800℃. The

yield strength increased from 530MPa for the base HEA to 614MPa for the Mo1.5 HEA. The strength of the W1.5 HEA and the (MoW)1.5 HEA also increased, but not as significant as Mo1.5 HEA. One possible explanation for the strength elevation is that molybdenum partitioned to the matrix phase more strongly than tungsten and imparted the most strength by solid solution hardening. The stacking fault energy is lowered after alloying with refractory ele- ments[23], which possibly makes it more difficult for the dissociated dislocations to cross slip.

4. Discussion

4.1 The partitioning behavior of refractory elements

γ' precipitates are Cu_3Au-type intermetallic compounds with mainly Ni and Co atoms occupying the face-centered positions (A sites in A_3Btype $L1_2$ phase) of the cubic cell, and Al and Ti atoms occupying the cubic corners (B sites in A_3B-type $L1_2$ phase)[9]. As a result, the total atomic percentage of Ni + Co is close to 75 at.% and Al + Ti close to 25 at.% in the precipitates. Previous first-principle calculations[9] suggested that Fe atoms prefer to occupy the cubic face centers. Moreover, in the Cr-modified Co–30Ni–10Al–5Mo–2Ta–2Ti-*x*Cr ($x=0,2,5,8$ at.%) HEAs[49], spatial distribution maps generated from APT suggested that Cr took the corner positions first at a low Cr concentration ($x=2,5$ at.%), then face-centered positions at a high Cr concentration ($x=8$ at.%). Therefore, it is identified the precipitates among the base HEA as the $(Ni_{47.7}Co_{22.1}Fe_{5.1}Cr_{0.1})_3(Al_{9.6}Ti_{12.4}Cr_3)$ phase.

W is regarded as a precipitation-former element in Co-based super- alloys, substituting for atoms at the cubic corner positions[12]. For example, W partitioned to the precipitation in the ternary Co–7Al–7W alloy with a high degree (K_W = 6.2)[42]. Alloying 25 at.% Ni to Co-based superalloys suppressed K_W from 6.2 to 1.07[50]. W parti- tioned to the precipitation in the W1.5 HEA, but with a much less extent (K_W = 1.52). The suppression of K_W after Ni alloying can be attributed to the matrix transformation from the pure γ-Co matrix (in Co–Al–W su- peralloys) to the (Co, Ni)-rich matrix (in the W1.5 HEA) and the Ni in the matrix solid solution with more tungsten. Mo partitioned to the γ matrix (K_{Mo} 0.46) in Mo1.5 HEA, but the partitioning coefficient of Mo varied over a large range, depending on the overall alloy compositions and aging temperatures[31,51]. First-principle calculations pointed out that both Mo and W atoms share the same sublattice sites in γ' precipitates, that is the cubic corner positions [52]. According to the TEM-EDX data, the compositions of the γ' precipitates are determined as the $(Ni_{47.6}C\text{-}o_{20.8}Fe_{4.3}Cr_{2.3})_3(Al_{10.1}Ti_{13.3}Cr_{1.0}Mo_{0.60})$ phase for Mo1.5 HEA, the $(Ni_{45.2}Co_{24.1}Fe_{5.5}Cr_{0.2})_3(Al_{8.7}Ti_{11.1}Cr_{3.2}W_{2.0})$ phase for W1.5 HEA, and the $(Ni_{45.2}Co_{23.6}Fe_{5.6}Cr_{0.6})_3(Al_{9.7}Ti_{10.8}Cr_{3.1}Mo_{0.3}W_{1.1})$ phase for (MoW) 1.5 HEA, respectively.

The reversal partitioning effects can be explained by the multi- species interactions among multicomponent alloys[53,54]. For example, Ru is known to reverse the partitioning behavior of Re from the γ matrix to γ' precipitates[53]. Since the formation of TCP phase in superalloys can be ascribed to the Re supersaturation in the γ matrix phase, the Re concentrations in the γ matrix phase can be suppressed due to such

reverse Re partitioning, making Re unavailable for TCP phase formation. It is also reported that W, usually partitioned to the γ' phase in the ternary Ni–Al–W alloys (K_W = 1.49), would repartition to the γ phase in multicomponent Ni-based superalloys (K_W = 0.92 for ME-9 and K_W = 0.89 for ME-15)[54]. Ta atoms, which had a stronger affinity for γ' precipitates, could push W atoms to the γ phase because Ta atoms occupied the same sublattice sites as W. In this study, since both Mo and W atoms occupy the same corner positions in the $L1_2$-type γ' precipitates[52], it is anticipated the competing site occupation behavior for Mo and W atoms after the combined Mo and W alloying. Part of the W atoms which used to take the corner positions in the γ' precipitates of W1.5 HEA were rejected to the γ matrix phase in (MoW)1.5 HEA with the presence of Mo, leading to the reversal W partitioning behavior from γ' precipitates (K_W 1.54 for W1.5 HEA) to the γ matrix (K_W 0.92 for (MoW)1.5 HEA). It is concluded that the W partition is sensitive to the Mo concentration.

4.2 The alloying effect of refractory elements on microstructural evolution

For microstructural evolution, precipitates retained spheroidal at the early stage of coarsening (Fig. 2). But precipitates became cuboidal with rounded corners in the later stage of aging, especially for the base HEA after aging for 336h. The sphere-to-cube morphological transition has also been reported in Ni-based superalloys[22,55]. This morphological evolution is governed by the competition between the interfacial energy and the elastic interactions between the γ and γ' phases. The size of the precipitates was small at the beginning of aging. Interfacial energies dominated this stage because

of the large specific surface area, leading to a spheroidal precipitation with the minimization of interfacial energy. As the precipitates grow, the elastic energy increases in proportion to the cube of precipitation radius, whereas the interfacial energy increases only in a square manner. As a result, to accommodate the difference in the lattice parameters of the γ and γ' phase, the elastic energy takes a leading role in the later coarsening stage. In order to reconcile the contributions from the interfacial energy and elastic energy, the L parameter was brought out by Thompson as[56]:

$$L = \frac{\varepsilon^2 C_{44}}{\sigma} r \tag{8}$$

where ε is the lattice parameter misfit strain and can be calculated as $\varepsilon = (a_{\gamma} - a_{\gamma})/a_{\gamma}$ (where $a_{\gamma'}$ and a_{γ} are the lattice parameters for the γ' and γ phase, respectively), C_{44} is an elastic constant of the γ matrix, σ is the interfacial energy, and γ is the radius of the precipitates. It suggests a morphology transition from spherical shape at the small precipitation size, to a 4-fold symmetric shape at the intermediate size when $2 < L < 4$, finally to a 2-fold symmetric shape with an alignment along the elastically soft [100] direction when $L > 5.6$.

In order to calculate the L parameter, ε is calculated according to the lattice parameters gained by XRD (Fig. 6). The values of elastic constant C_{44} and interfacial energy σ is estimated as 144GPa[57] and 19 mJ/m^2[58]. After substituting all the values into equation (8), the parameter L is calculated to be 4.3 for the base HEA, 2.4 for the Mo1.5 HEA, 3.0 for the W1.5 HEA, and 2.2 for the (MoW)1.5 HEA after the 336 h aging. The well-aligned precipitation in the base HEA and W1.5 HEA along one axis can be clearly identified in Fig. 2. Although the calculated L parameter of the base HEA and the W1.5 HEA is smaller than the predicted threshold value of 5.6, discrepancies from

the experimental observation can be a result of an inaccurate estimation of elastic constant and interfacial energy for PH-HEAs. For the Mo1.5 HEA and (MoW)1.5 HEAs, the precipitates show no sign of alignment and remain randomly distributed. Such observation matched well with the Thompson's theory[56], which confirmed that the influence from the altered lattice misfit to the precipitation morphology evolution.

4.3 The alloying effect of refractory elements on the coarsening kinetics and mechanism

The temporal evolution of precipitates size for the base, Mo1.5, W1.5, and (MoW)1.5 HEAs aging at 800°C is shown in Fig. 9a. Multiple regression analyses were applied to the plot in order to solve the temporal exponent of the average precipitation size (Fig. 9a). The slope of log(r) versus log(t) yielded the temporal exponent of 0.319 ± 0.048, 0.315 ± 0.052, 0.338 ± 0.041, and 0.301 ± 0.034 for the base, Mo1.5, W1.5, and (MoW)1.5 HEAs, respectively. All these temporal exponents for the four HEAs are close to the value of 1/3, as predicted by the Lifshitz-Slyozov-Wagner (LSW) [32], Kuehman-Voorhees (KV)[37], and Philippe-Voorhees (PV) coarsening model[35], which implies that the coarsening behavior in these alloys is controlled by a solute diffusion. Linear regression analyses of the plot between r^3 and aging time yielded the slope equal to the coarsening rate constant (Fig. 9b). The base HEA shows the largest coarsening rate among all these four PH-HEAs ($7.571 \pm 0.948 \times 10^{-29} m^3/s$). With the alloying addition of Mo or W refractory elements, the coarsening rate decreased to $7.087 \pm 1.073 \times 10^{-29}$ and $6.984 \pm 0.744 \times 10^{-29} m^3/s$ for Mo1.5 and W1.5 HEAs, respectively. By comparison, the (MoW)1.5 HEA exhibits the smallest coarsening rate of $6.239 \pm 0.603 \times 10^{-29} m^3/s$. Microstructural stability is a necessity for high-temperature applications since a fast

precipitation coarsening results in a degradation of mechanical properties, thus a comparison be- tween HEAs and traditional superalloys is important. The coarsening rate of the four measured HEAs is lower than conventional superalloys, either Ni-based superalloys ($8.7\times10^{-28}m^3/s$ for Ni-9.7Al-8.5Cr-2.0W[22]) or Co-based superalloys ($1.2\times10^{-28}m^3/s$ for Co-9.9Ni-8.8Al-8.9W[39]). It indicates that the coarsening resistance of the current high-entropy alloys is significantly better than that of con- ventional superalloys.

Assuming element i is the rate-determining specimen, the coarsening rate constant K_r can be derived according to the modified-LSW theory as[36]:

$$K_r = \frac{8D_i\sigma C_i^{\gamma}\left(1-C_i^{\gamma}\right)v_m}{9RT\left(C_i^{\gamma'}-C_i^{\gamma}\right)^2} \tag{9}$$

where D_i is the diffusivity of element i , σ is the interfacial energy between the matrix and the precipitates, C_i^{γ} and $C_i^{\gamma'}$ is the equilibrium concentration of element i in the γ and γ' phase, respectively, v_m is the mole volume of the precipitation, R is the gas constant, and T is the thermodynamic temperature. According to this model, the coarsening rate constant is a function of : (i) diffusivity of the controlling solute element D_i , (ii) interfacial energy between the matrix and the precipitates σ and (iii) elemental concentration $C_i^{\gamma'}$ and C_i^{γ} .

Because of the large atomic size of the alloyed molybdenum atoms (0.136nm) and tungsten atoms (0.137nm), as compared with that of nickel (0.125nm) and cobalt atoms (0.125nm)[59], the diffusion coefficient of Mo and W is small[60]. To quantitatively evaluate the effect of the low diffusivity of the refractory elements, the diffusion coefficient of various solute atoms should be evaluated. Due to the highly concentrated

Co in the γ phase, the diffusion coefficient of alloying el- ements is calculated by extrapolating the diffusion parameters in the γ-Co phase[61–66]. The solute diffusivities of Ni, Co, Fe, Cr, Al, and Ti are determined to be 7.17×10^{-18}, 5.98×10^{-18}, 1.30×10^{-17}, 4.57×10^{-18}, and $3.51\times10^{-17}\,m^2/s$, respectively. The diffusivities of the refractory elements of Mo and W are calculated as 3.63×10^{-18} and $2.07\times10^{-18}\,m^2/s$, respectively. Evidently, the W element is the slowest diffusing solute and the diffusion of Mo is slightly faster than that of W. So, either Mo or W atoms control the coarsening after alloy- ing, which accounts for the slower coarsening rate.

Both lattice misfit and segregation of refractory elements at the interface alter the interfacial energy and exert an influence on the coarsening behavior. Lattice misfit induces the elastic stress at the interface. It is argued that the value of the lattice misfit δ close to zero minimizes the interfacial energy, thus the coarsening can be slowed down[67]. The smallest lattice misfit in (MoW)1.5 HEA may contribute to the microstructural stability by maintaining the smallest elastic stress during the coarsening process. In order to investigate the possible elemental segregation at the γ/γ' interface, APT was utilized to investigate the elemental profile at the γ/γ' interface. Fig. 10a illustrated the three-dimensional reconstruction of the MoW1.5 HEA after 336 h aging at 800℃. The narrow γ matrix channel is sandwiched between two γ' precipitates. The elemental partitioning behavior across the interface between the γ and γ' phases is shown in the concentration profiles for the solutes (Fig. 10b). The elemental partitoning behavior obtained from APT reconstruction matches that obtained from TEM-EDX analysis (Fig. 3c), with Ni, Al, and Ti preferential partitoned to the

precipitates and Co, Fe, and Cr partitioned to the matrix. Mo partitioned to the matrix, and tungsten distributed evenly between the two phases, as showed in Fig. 10c. However, there is no evidence showing the local segregation of refractory elements at the interface region, which is different from the case as found among Ni-base superalloy René N6[68] and CoNi-base superalloy Co–30Ni–10Al–5Mo–2Nb-2Re (at.%)[31]. The results suggest that the segregation of refractory elements at the interface may be a result of complicated atomic interactions among the solutes[72]. Since solute segregation is driven by the thermodynamic Gibbs free energy reduction in a spatially confined manner, locally ltered chemical composition at the γ/γ' interface controls the solute segregation. A possible explanation is that solute segregation at the interface was not thermodynamically favourable in the multicomponent HEA we currently studied, but it is preferred among above-mentione Ni-based or CoNi-based superalloys. In-depth atomistic understanding of this behaviour will be conducted in the future. As a result, we did not find any evidence showing solute segregation. In this way, the possibility of the reduced interfacial energy as a result of interfacial elemental segregation is elimiated. The minimized lattice misfit after reractory elements alloyi ng accounts for the decreased in terfacial energy.

4.4 Mechanical behaviors

Mechanical properties are closely related to the interactions between dislocations and precipitates. The dislocation-precipitate interactions can be divided into two

different mechanisms: precipitation shearing mechanism and Orowan dislocation looping mechanism. Particle shearing mechanism usually works for small particles, whereas the dislocation looping mechanism dominates for large particles. As the particle grows, the shear stress required for shearing increases. As a result, a critical precipitation size can be determined for the shearing- looping transition.

For precipitation shearing mechanism, the shear stress, $\Delta\tau$, required can be calculated as[69]:

$$\Delta\tau_{\text{shear}} = \frac{1}{2}\left(\frac{\gamma_{\text{APB}}}{b}\right)^{\frac{3}{2}}\left(\frac{2rb\varphi}{\gamma}\right)^{\frac{1}{2}}A - \frac{1}{2}\left(\frac{\gamma_{\text{APB}}}{b}\right)\varphi \tag{10}$$

where γ_{APB} is the anti-phase boundary energy of the precipitate, r is precipitate radius, b is the Burgers vector of the dislocation, φ is the volume fraction of the precipitate, r is the dislocation line tension, and A is a numerical morphological factor.

The anti-phase boundary energy γ_{APB} is estimated to be 0.3 J/m^2 which is taken from Ni-base superalloys[70], Burgers vector of the dislocation $b = \frac{\sqrt{2}}{2}a$ (a Is the lattice parameter of the matrix) , γ can be estimated as $\frac{1}{2}Gb^2$ [71] ($G = 78.5$ Gpa is the shear modulus of the matrix[61]), and A equals 0.72 for spherical particles[69].

The Orowan looping mechanism involves the dislocation looping around the precipitation, and the additional stress required for looping is given as[70]:

$$\Delta\tau_{\text{orowan}} = \frac{0.81Gb\ln\left(\frac{2r}{b}\right)}{4\pi r\left(\sqrt{\frac{\pi}{4\varphi}-1}\right)\sqrt{1-\nu}} \tag{11}$$

where $v = 0.31$ is the Poisson's ration[6].

The additional stress required for precipitate shearing mechanism and Orowan looping mechanism as a function of precipitation size is calculated and shown in Fig. 11. Since the two mechanisms work independently, the stress increment is determined by the smaller stress required among the two competing mechanisms. There is an optimal precipitate size range and the largest strength elevation can be obtained at a precipitation radius at around 30nm, and such largest strength can be used to explain the reason for the peak hardness after 168h aging at 800℃. The precipitation size was around 30nm after 168h aging (Table 1), which is roughly corresponding to the caculated optimum precipitation size. Based on the measured particle size and the calculated stress level, we conclude that dislocations inter with precipitates essentially by shearing through before the peak, and the Orowan looping becomes the operative mechanism after the peak.

5. Conclusions

The present work demonstrates the potential for the refractory- element alloyed PH-HEAs to be used as high-temperature structural materials. The findings in this study can be summarized as:

1) Aging at 800℃ induced the formation of ordered $L1_2$-type precipitates in this study. The $L1_2$-type precipitate was identified to be a (Ni, Al, Ti)-rich ordered phase, while the matrix is a (Fe, Co, Cr)-rich disordered fcc phase. Mo partitioned mainly with the matrix

phase in both the Mo1.5 and (MoW)1.5 HEA. W partitioned to precipitates in the W1.5 HEA with a partitioning coefficient of 1.52 but reparti- tioned to the matrix phase in the (MoW)1.5 HEA. Such reverse partition behavior of W can be attrib uted to the elemental in- teractions between Mo and W atoms. The volume fraction of $L1_2$-type precipitation was 38.8% for the base HEA and 36.5% for the (MoW) 1.5 HEA. Alloying Mo slightly reduced it to 34.5%, whereas W increased it to 41.2%. A sphere-to-cube morphological transition was observed with the prolongation of aging time. In particular, the wellaligned precipitation morphology formed only in the base and W1.5 HEA after 336h aging due to the competing interfacial energy and elastic energy.

2) Isothermal heat treatments led to the Heusler phase formation. Mo and W displayed different effects on the formation of Heusler phase. Basically, Mo promoted its formation, whereas W destabilized Heusler phase.

3) Positive lattice misfit was maintained among all the four PH-HEAs at room temperature. Alloying refractory elements effectively reduced the lattice misfit from 0.3549% for the base HEA to 0.2702%, 0.3032%, and 0.2642% for the Mo1.5 HEA, W1.5 HEA, and (MoW) 1.5 HEA, respectively. The lattice misfit in the (MoW)1.5 HEA was the smallest, which can be ascribed to the reversed partitioning behavior of W.

4) PH-HEAs exhibited a superior coarsening resistance than that of conventional Ni- and Co-base superalloys because the coarsening rate constant of PH-HEAs in this study was smaller than that of conventional superalloys. (MoW)1.5 HEA outperformed all the other HEAs in the aspect of coarsening resistance. Either the intrinsic small diffusivities

of the refractory elements or the reduced interfacial energy contributed to a superior thermal stability after alloying with refractory additions.

5) Alloying refractory elements to PH-HEAs improved the high-temperature yield strength. The microhardness at room temperature peaked around 168 h aging at 800℃. It is anticipated that the dislocation-precipitation interactions transform from the dislocation shearing mechanism before the peak to the Orowan dislocation looping mechanism after such peak.

CRediT authorship contribution statement

B.X. Cao: Conceptualization, Methodology, Investigation, Writing - original draft. **T. Yang:** Conceptualization, Methodology, Investigation. **L. Fan:** Investigation. **J.H. Luan:** Investigation. **Z.B. Jiao:** Funding acquisition. **C.T. Liu:** Conceptualization, Supervision, Funding acquisi- tion, Project administration.

Declaration of competing interest

The authors declare that they have no known competing financial interests or personal relationships that could have appeared to influence the work reported in this paper.

Acknowledgement

The authors from City University of Hong Kong (CityU) are grateful for the financial support from the Hong Kong Research Grant Council (RGC) with CityU Grant 11213319, 11202718, and 25202719. The au- thors from The Hong Kong Polytechnic University (PolyU) are grateful for the financial support from the Hong Kong RGC (25202719), the National Natural Science Foundation of China (NSFC 51801169), and PolyU-CNERC (P0013862).

References

1. B. Gludovatz, A. Hohenwarter, D. Catoor, E.H. Chang, E.P. George, R.O. Ritchie, A fracture-resistant high-entropy alloy for cryogenic applications, Science 345

(2014) 1153–1158.

2. F. Otto, A. Dlouhý, C. Somsen, H. Bei, G. Eggeler, E.P. George, The influences of temperature and microstructure on the tensile properties of a CoCrFeMnNi high-entropy alloy, Acta Mater 61 (2013) 5743–5755.

3. B. Cantor, I. Chang, P. Knight, A. Vincent, Microstructural development in equiatomic multicomponent alloys, Mater. Sci. Eng., A 375 (2004) 213–218.

4. J.W. Yeh, S.K. Chen, S.J. Lin, J.Y. Gan, T.S. Chin, T.T. Shun, C.H. Tsau, S.Y. Chang, Nanostructured high-entropy alloys with multiple principal elements: novel alloy design concepts and outcomes, Adv. Eng. Mater. 6 (2004) 299–303.

5. B. Cao, C. Wang, T. Yang, C. Liu, Cocktail effects in understanding the stability and properties of face-centered-cubic high-entropy alloys at ambient and cryogenic temperatures, Scripta Mater. 187 (2020) 250–255.

6. J. He, H. Wang, H. Huang, X. Xu, M. Chen, Y. Wu, X. Liu, T. Nieh, K. An, Z. Lu, A precipitation-hardened high-entropy alloy with outstanding tensile properties, Acta Mater 102 (2016) 187–196.

7. B. Gwalani, V. Soni, D. Choudhuri, M. Lee, J. Hwang, S. Nam, H. Ryu, S.H. Hong, R. Banerjee, Stability of ordered L12 and B2 precipitates in face centered cubic based high entropy alloys-Al0. 3CoFeCrNi and Al0. 3CuFeCrNi2, Scripta Mater. 123 (2016) 130–134.

8. Y. Zhao, T. Yang, Y. Tong, J. Wang, J. Luan, Z. Jiao, D. Chen, Y. Yang, A. Hu, C. T. Liu, Heterogeneous precipitation behavior and stacking-fault-mediated deformation in a CoCrNi-based medium-entropy alloy, Acta Mater 138 (2017) 72–82.

9. T. Yang, Y. Zhao, Y. Tong, Z. Jiao, J. Wei, J. Cai, X. Han, D. Chen, A. Hu, J.J. Kai, C. T. Liu, Multicomponent intermetallic nanoparticles and superb mechanical behaviors of complex alloys, Science 362 (2018) 933–937.

10. C.T. Sims, N.S. Stoloff, W.C. Hagel, Superalloys II, Wiley, New York, 1987.

11. E. Nembach, G. Neite, Precipitation hardening of superalloys by ordered γ'-particles, Prog. Mater. Sci. 29 (1985) 177–319.

12 J. Sato, T. Omori, K. Oikawa, I. Ohnuma, R. Kainuma, K. Ishida, Cobalt-base high- temperature alloys, Science 312 (2006) 90–91.

13 W. Walston, K. O'hara, E. Ross, T. Pollock, W. Murphy, RENE N6: THIRD GENERATION SINGLE CRYSTAL SUPERALLOY, 1996.

14. K. Kawagishi, A.C. Yeh, T. Yokokawa, T. Kobayashi, Y. Koizumi, H. Harada, Development of an oxidation-resistant high-strength sixth-generation single-crystal superalloy TMS-238, Proceedings of Superalloys 2012 (2012) 9–13.

15. P. Pandey, S. Kashyap, D. Palanisamy, A. Sharma, K. Chattopadhyay, On the high temperature coarsening kinetics of γ’ precipitates in a high strength

16. $Co_{37.6}Ni_{35.4}Al_{9.9}Mo_{4.9}Cr_{5.9}Ta_{2.8}Ti_{3.5}$ fcc-based high entropy alloy, Acta Mater 177 (2019) 82–95.

17. J. Chen, X. Zhou, W. Wang, B. Liu, Y. Lv, W. Yang, D. Xu, Y. Liu, A review on fundamental of high entropy alloys with promising high–temperature properties, J. Alloys Compd. 760 (2018) 15–30.

18. T. Tsao, A. Yeh, C. Kuo, K. Kakehi, H. Murakami, J. Yeh, S. Jian, The high temperature tensile and creep behaviors of high entropy superalloy, Sci. Rep. 7 (2017) 12658.

19. B. Cao, T. Yang, W. Liu, C. Liu, Precipitation-hardened high-entropy alloys for high-temperature applications: a critical review, MRS Bull 44 (2019) 854–859.

20. J.H. Perepezko, The hotter the engine, the better, Science 326 (2009) 1068–1069.

21. B. Geddes, H. Leon, X. Huang, Superalloys: Alloying and Performance Asm International, 2010.

22. A. Giamei, D. Anton, Rhenium additions to a Ni-base superalloy: effects on microstructure, Metall. Mater. Trans. A 16 (1985) 1997–2005. C.K. Sudbrack, T.D. Ziebell, R.D. Noebe, D.N. Seidman, Effects of a tungsten addition on the morphological evolution, spatial correlations and temporal evolution of a model Ni–Al–Cr superalloy, Acta Mater 56 (2008) 448–463.

23. E. Fleischmann, M.K. Miller, E. Affeldt, U. Glatzel, Quantitative experimental determination of the solid solution hardening potential of rhenium, tungsten and molybdenum in single-crystal nickel-based superalloys, Acta Mater 87 (2015) 350–356.

24. K. Kawagishi, H. Harada, A. Sato, A. Sato, T. Kobayashi, The oxidation properties of fourth generation single-crystal nickel-based superalloys, Jom 58 (2006) 43–46.

25 C.M. Rae, R.C. Reed, The precipitation of topologically close-packed phases in rhenium-containing superalloys, Acta Mater 49 (2001) 4113–4125.

26. P.J. Fink, J.L. Miller, D.G. Konitzer, Rhenium reduction-alloy design using an economically strategic element, Jom 62 (2010) 55–57.

27. W. Loomis, J. Freeman, D. Sponseller, The influence of molybdenum on the γ’ phase in experimental nickel-base superalloys, Metall. Mater. Trans. B 3 (1972) 989–1000.

28. V. Biss, D. Sponseller, The effect of molybdenum on γ’ coarsening and on

elevated- temperature hardness in some experimental nickel-base superalloys, Metall. Trans. 4 (1973) 1953–1960.

29. J.P. Collier, P.W. Keefe, J.K. Tien, The effects of replacing the refractory elements W, Nb, and Ta with Mo in nickel-base superalloys on microstructural, microchemistry, and mechanical properties, Metall. Trans. A 17 (1986) 651–661.

30. C.Y. Hsu, C.C. Juan, S.T. Chen, T.S. Sheu, J.W. Yeh, S.K. Chen, Phase diagrams of high-entropy alloy system Al-Co-Cr-Fe-Mo-Ni, Jom 65 (2013) 1829–1839.

31. P. Pandey, A.K. Sawant, B. Nithin, Z. Peng, S. Makineni, B. Gault, K. Chattopadhyay, On the effect of Re addition on microstructural evolution of a CoNi-based superalloy, Acta Mater 168 (2019) 37–51.

32 I.M. Lifshitz, V.V. Slyozov, The kinetics of precipitation from supersaturated solid solutions, J. Phys. Chem. Solid. 19 (1961) 35–50.

33 C. Wagner, Theory of precipitate change by redissolution, Z. Elektrochem 65 (1961) 581–591.

34 S. Bjo¨rklund, L. Donaghey, M. Hillert, The effect of alloying elements on the rate of Ostwald ripening of cementite in steel, Acta Metall 20 (1972) 867–874.

35 A. Umantsev, G.B. Olson, Ostwald ripening in multicomponent alloys, Scripta Metall. 29 (1993).

36 H. Calderon, P.W. Voorhees, J. Murray, G. Kostorz, Ostwald ripening in concentrated alloys, Acta Metall. Mater. 42 (1994) 991–1000.

37. C. Kuehmann, P.W. Voorhees, Ostwald ripening in ternary alloys, Metall. Mater. Trans. A 27 (1996) 937–943.

38 A.J. Ardell, V. Ozolins, Trans-interface diffusion-controlled coarsening, Nat. Mater. 4 (2005) 309.

39. D.J. Sauza, D.C. Dunand, R.D. Noebe, D.N. Seidman, γ'-(L12) precipitate evolution during isothermal aging of a CoAlWNi superalloy, Acta Mater 164 (2019) 654–662.

40 K. Song, M. Aindow, Grain growth and particle pinning in a model Ni-based superalloy, Mater. Sci. Eng. 479 (2008) 365–372.

41. X. Liu, L. Wang, L. Lou, J. Zhang, Effect of Mo addition on microstructural characteristics in a Re-containing single crystal superalloy, J. Mater. Sci. Technol. 31 (2015) 143–147.

42. S. Meher, R. Banerjee, Partitioning and site occupancy of Ta and Mo in Co-base γ/γ' alloys studied by atom probe tomography, Intermetallics 49 (2014) 138–142.

43 M. Nathal, R. MacKay, R. Garlick, Temperature dependence of γ-γ’ lattice mismatch in nickel-base superalloys, Mater. Sci. Eng. 75 (1985) 195–205.

44. H. Mughrabi, The importance of sign and magnitude of γ/γ’ lattice misfit in superalloys—with special reference to the new γ’-hardened cobalt-base superalloys, Acta Mater 81 (2014) 21–29.

45 J. Svoboda, P. Luka´ˇs, Model of creep in <001>-oriented superalloy single crystals, Acta Mater 46 (1998) 3421–3431.

46. L. Lu, R. Schwaiger, Z. Shan, M. Dao, K. Lu, S. Suresh, Nano-sized twins induce high rate sensitivity of flow stress in pure copper, Acta Mater 53 (2005) 2169–2179.

47. X. An, S. Wu, Z. Zhang, R. Figueiredo, N. Gao, T. Langdon, Evolution of microstructural homogeneity in copper processed by high-pressure torsion, Scripta Mater. 63 (2010) 560–563.

48. D. Tabor, The Hardness of Metals, Oxford university press, 2000.

49. P. Pandey, S.K. Makineni, A. Samanta, A. Sharma, S.M. Das, B. Nithin,

C. Srivastava, A.K. Singh, D. Raabe, B. Gault, Elemental site occupancy in the L12 A3B ordered intermetallic phase in Co-based superalloys and its influence on the microstructure, Acta Mater 163 (2019) 140–153.

50. K. Shinagawa, T. Omori, J. Sato, K. Oikawa, I. Ohnuma, R. Kainuma, K. Ishida, Phase equilibria and microstructure on γ’ phase in Co-Ni-Al-W system, Mater. Trans. 49 (2008) 1474–1479.

51. C. Jia, K. Ishida, T. Nishizawa, Partition of alloying elements between γ (A1), γ’(L12), and β (B2) phases in Ni-Al base systems, Metall. Mater. Trans. A 25 (1994) 473–485.

52. Q. Wu, S. Li, Alloying element additions to Ni3Al: site preferences and effects on elastic properties from first-principles calculations, Comput. Mater. Sci. 53 (2012) 436–443.

53. A. Volek, F. Pyczak, R. Singer, H. Mughrabi, Partitioning of Re between γ and γ’ phase in nickel-base superalloys, Scripta Mater. 52 (2005) 141–145.

54. Y. Amouyal, Z. Mao, D.N. Seidman, Effects of tantalum on the partitioning of tungsten between the γ and γ’ phases in nickel-based superalloys: linking experimental and computational approaches, Acta Mater 58 (2010) 5898–5911.

55. M. Fa¨hrmann, P. Fratzl, O. Paris, E. F¨ahrmann, W.C. Johnson, Influence of coherency stress on microstructural evolution in model Ni-Al-Mo alloys, Acta Metall. Mater. 43 (1995) 1007–1022.

56. M. Thompson, C. Su, P.W. Voorhees, The equilibrium shape of a misfitting precipitate, Acta Metall. Mater. 42 (1994) 2107–2122.

57. D. Siebo¨rger, H. Knake, U. Glatzel, Temperature dependence of the elastic moduli of the nickel-base superalloy CMSX-4 and its isolated phases, Mater. Sci. Eng., A 298 (2001) 26–33.

58 S. Meher, S. Nag, J. Tiley, A. Goel, R. Banerjee, Coarsening kinetics of γ' precipitates in cobalt-base alloys, Acta Mater 61 (2013) 4266–4276.

59. A. Takeuchi, A. Inoue, Classification of bulk metallic glasses by atomic size difference, heat of mixing and period of constituent elements and its application to characterization of the main alloying element, Mater. Trans. 46 (2005) 2817–2829.

60 G. Hood, An atom size effect in tracer diffusion, J. Phys. F Met. Phys. 8 (1978) 1677.

61. A. Bristoti, A. Wazzan, Diffusion of zinc and iron in pure cobalt and diffusion of iron in two iron-cobalt alloys, Rev. Bras. Fis 4 (1974) 1–10.

62. A. Davin, V. Leroy, D. Coutsouradis, L. Habraken, Diffusion de quelques ´el´ements de substitution dans le fer, le nickel et le cobalt, Memoires Scientifiques Rev Metall 60 (1963) 275–283.

63. A. Green, N. Swindells, Measurement of interdiffusion coefficients in Co–Al and Ni–Al systems between 1000 and 1200 C, Mater Sci Tech-Lond 1 (1985) 101–103.

64. K.i. Hirano, R. Agarwala, B. Averbach, M. Cohen, Diffusion in cobalt-nickel alloys, J. Appl. Phys. 33 (1962) 3049–3054.

65. T. Ustad, H. Sørum, Interdiffusion in the Fe-Ni, Ni-Co, and Fe-Co systems, Phys. Status Solidi 20 (1973) 285–294.

66. P.J. van der Straten, G.F. Bastin, F.J. van Loo, G.D. Rieck, Phase equilibria and interdiffusion in the cobalt-titanium system, Zeitschrift fuer Metallkunde 67 (1976) 152–157.

67. R. Ecob, A. Porter, R. Ricks, The measurement of precipitate/matrix lattice mismatch in nickel-base superalloys, Scripta Metall. 16 (1982) 1085–1090.

68. K.E. Yoon, R.D. Noebe, O.C. Hellman, D.N. Seidman, Dependence of interfacial excess on the threshold value of the isoconcentration surface, Surf. Interface Anal. 36 (2004) 594–597.

69. B. Reppich, Some new aspects concerning particle hardening mechanisms in γ' precipitating Ni-base alloys—I. Theoretical concept, Acta Metall 30 (1982) 87–94.

70. D. Raynor, J. Silcock, Strengthening mechanisms in γ' precipitating alloys,

Metal, Sci. J. 4 (1970) 121–130.

71. A. Kamara, A. Ardell, C. Wagner, Lattice misfits in four binary Ni-Base γ/γ' alloys at ambient and elevated temperatures, Metall. Mater. Trans. A 27 (1996) 2888–2896.

72. T. Yang, Y. Zhao, W. Li, C. Yu, J. Luan, D. Lin, L. Fan, Z. Jiao, W. Liu, J.J. Kai, C. T. Liu, Ultrahigh-strength and ductile superlattice alloys with nanoscale disordered interfaces, Science 369 (2020) 427–432.

Figure captions

Fig. 1. (a) The equilibrium phases and their mole fractions in the temperature range from 750°C to 1400°C for the base HEA. (b) The calculated γ' solvus tem- perature, γ solidus temperature and liquidus temperature for base, Mo1.5, W1.5, and (MoW)1.5 HEAs

Fig. 2. Secondary electron SEM of base HEA after aging at 800°C for (a) 24h, (b) 72h, (c) 168h, and (d) 336 h; Mo1.5 HEA after aging at 800°C for (e) 24h, (f) 72h, (g) 168h, and (h) 336h; W1.5 HEA after aging at 800°C for (i) 24h, (j) 72 h, (k) 168h, and (l) 336h; (MoW)1.5 HEA after aging at 800°C for (m) 24h, (n) 72h, (o) 168 h, and (p) 336 h. The microstructures illustrated the temporal evolution of $L1_2$-type precipitates.

Fig. 3. (a) Dark-field TEM reveals the high- density cuboidal precipitates with rounded corners embedded in the matrix after aging at 800°C for 336h. The diffraction pattern (DP) obtained along [011] zone is taken from Mo1.5 HEA after aging at 800°C for 336h. Red circles in the DP represent $L1_2$ structure superlattice diffraction. (b) TEM-EDX mapping of base HEA after aging at 800°C for 336h, showing the elemental partitioning behavior. (c) Partitioning coefficient of elements in HEAs after aging at 800°C for 336h. Ni, Al, and Ti showed a pref- erential partitioning behavior to γ' precipitation phase, but Co, Fe, and Cr partitioned into γ ma- trix phase. W partitioned to γ' phase in W1.5 HEA but repartitioned to γ phase in (MoW)1.5 HEA. (For interpretation of the references to color in this figure legend, the reader is referred to the Web version of this article.)

Fig. 4. Microstructure of samples (a) after recrystallization and (b) aged for 336h at 800°C, showing equiaxial grains for all the specimens. Grain growth is negligible during isothermal treatment at 800°C.

Fig. 5. (a) A comparison of the grain sizes before and after aging at 800°C for 336h. (b) The volume fraction of Heusler phase as measured by image extraction. (c) TEM-EDX mapping of grain boundary Heusler phase in the Mo1.5 HEA after aging at 800°C for 336h, showing the strong partitioning of Al and Ti in the Heusler phase. Inset is the diffraction patterns taken along $z=[111]$. (d) Volume fraction of $L1_2$-type precipitates of HEAs after aging at 800°C for 336h, calculated by the lever rules.

Fig. 6. X-ray diffractions and peak deconvolutions of (a) base HEA, (b) Mo1.5 HEA, (c) W1.5 HEA, and (d) (MoW)1.5 HEA after aging at 800°C for 336h. Peak asymmetry is attributed to the different lattice constant for the matrix and the precipitates.

Fig. 7. (a) Lattice parameters of γ′ and γ phase calculated from the deconvolution of the (311) diffraction peaks. (b) Lattice misfit between γ′ and γ phase for base, Mo1.5, W1.5,

and (MoW)1.5 HEAs after aging at 800℃ for 336h. The XRD test was conducted at room temperature.

Fig. 8. (a) Temporal evolution of the microhardness for base, Mo1.5, W1.5, and (MoW)1.5 HEAs aging at 800℃. (b) Yield strength at 800℃ of base, Mo1.5, W1.5, and (MoW)1.5 HEAs after aging at 800℃ for 24h.

Fig. 9. (a) The scatter plot between average precipitation size r_p (nm) and aging time (s). Both the average precipitation size and aging time are in the logarithmic scale. Regression analysis was applied to the scatter points (dotted line). The slope of the plot between log(r) and log(t) yields the temporal exponents (1/n) of average precipitation size. (b) The scatter plot of r_p^3 (nm^3) versus aging time (s). Linear regression analysis was applied to the scatter points for each HEA after various aging time (dotted line). The slope of the linear regression yields the coarsening rate constant K_r

Fig. 10. (a) APT reconstruction of the MoW1.5 HEA after 336 h aging at 800℃, showing a narrow γ matrix channel and two adjacent γ′ precipitates. (b) Elemental concentration profiles across the γ/γ′ interface. (c) Magnification view of the Mo and W proxigrams at the interface.

Fig. 11. Strength increment earned from the dislocation shearing and Orowan looping mechanisms versus precipitation size. The optimal radius for precipi- tation strengthening is around 30 nm, which can be attributed to the compe- tition between dislocation shearing mechanism and Orowan looping mechanism.

Fig 1

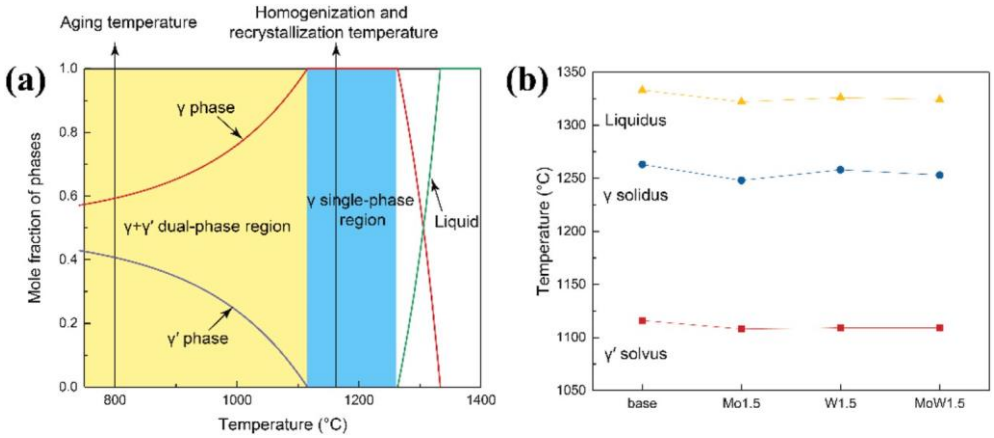
(a)
Aging temperature
Homogenization and recrystallization temperature
γ phase
γ+γ′ dual-phase region
γ single-phase region
Liquid
γ′ phase
Mole fraction of phases
Temperature (°C)
(b)
Liquidus
γ solidus
γ′ solvus
Temperature (°C)
base
Mo1.5
W1.5
MoW1.5

Fig 2

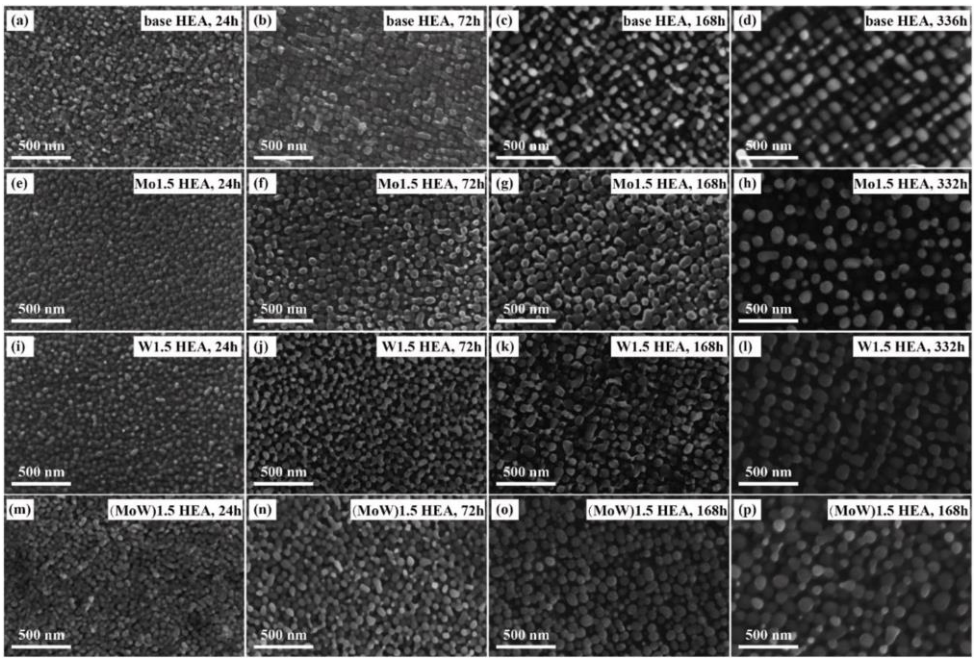
(a) base HEA, 24h
(b) base HEA, 72h
(c) base HEA, 168h
(d) base HEA, 336h
(e) Mo1.5 HEA, 24h
(f) Mo1.5 HEA, 72h
(g) Mo1.5 HEA, 168h
(h) Mo1.5 HEA, 332h
(i) W1.5 HEA, 24h
(j) W1.5 HEA, 72h
(k) W1.5 HEA, 168h
(l) W1.5 HEA, 332h
(m) (MoW)1.5 HEA, 24h
(n) (MoW)1.5 HEA, 72h
(o) (MoW)1.5 HEA, 168h
(p) (MoW)1.5 HEA, 168h
500 nm

Fig 3

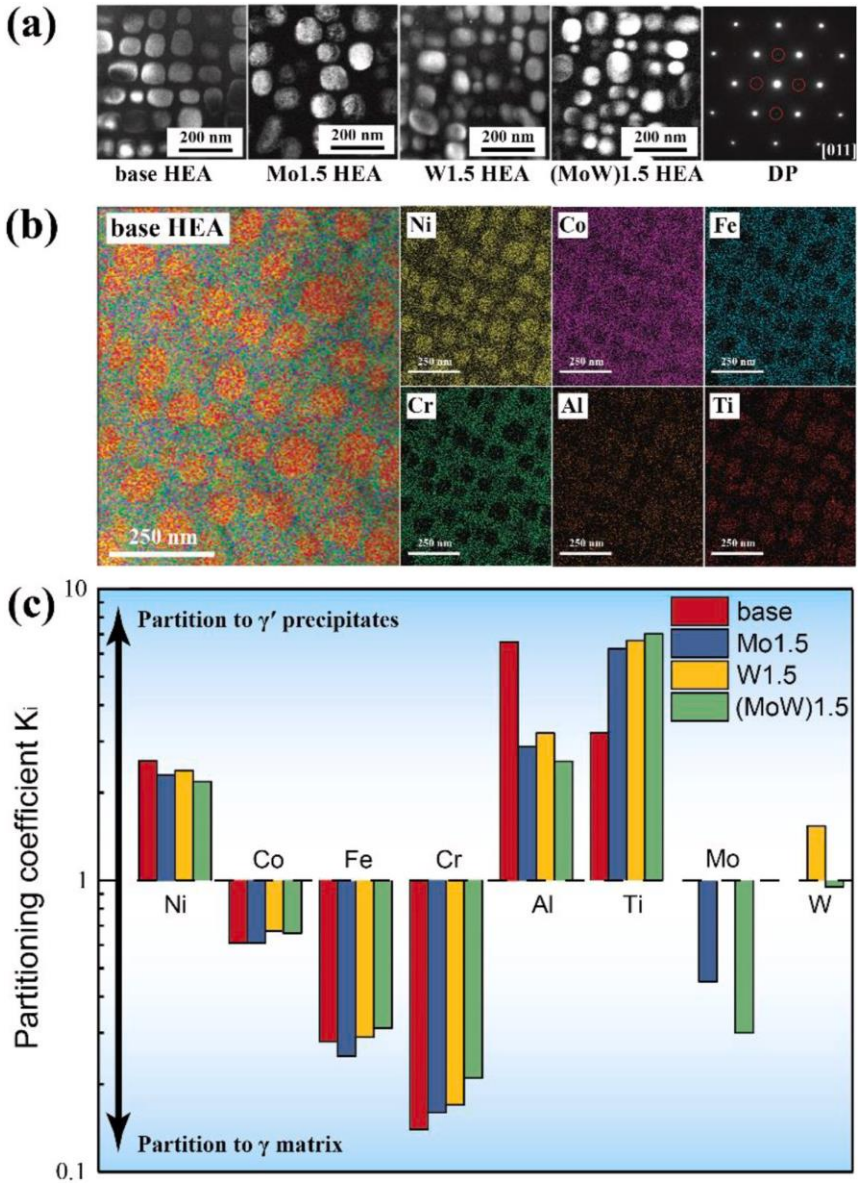
(a)
200 nm
200 nm
200 nm
200 nm
[011]
base HEA
Mo1.5 HEA
W1.5 HEA
(MoW)1.5 HEA
DP
(b)
base HEA
250 nm
Ni
Co
Fe
Cr
Al
Ti
(c)
Partitioning coefficient Ki
10
1
0.1
Partition to γ′ precipitates
Partition to γ matrix
base
Mo1.5
W1.5
(MoW)1.5
Ni
Co
Fe
Cr
Al
Ti
Mo
W

Fig 4

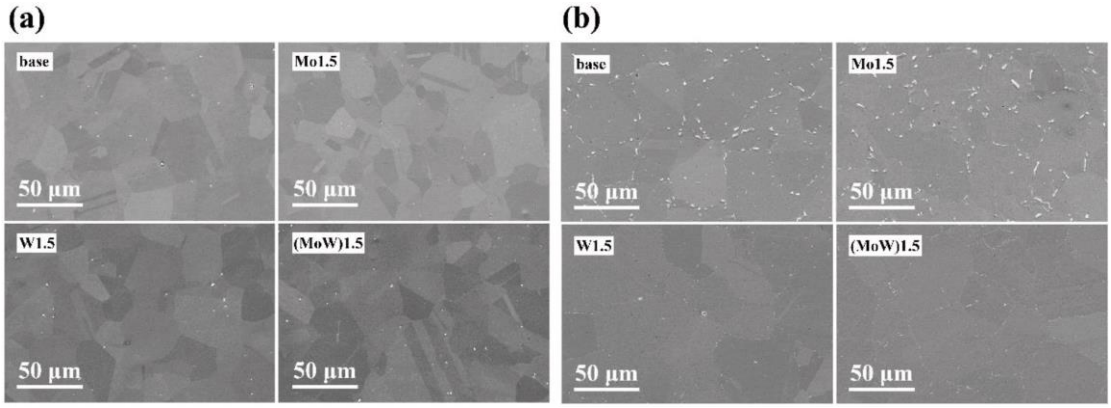

Fig 5

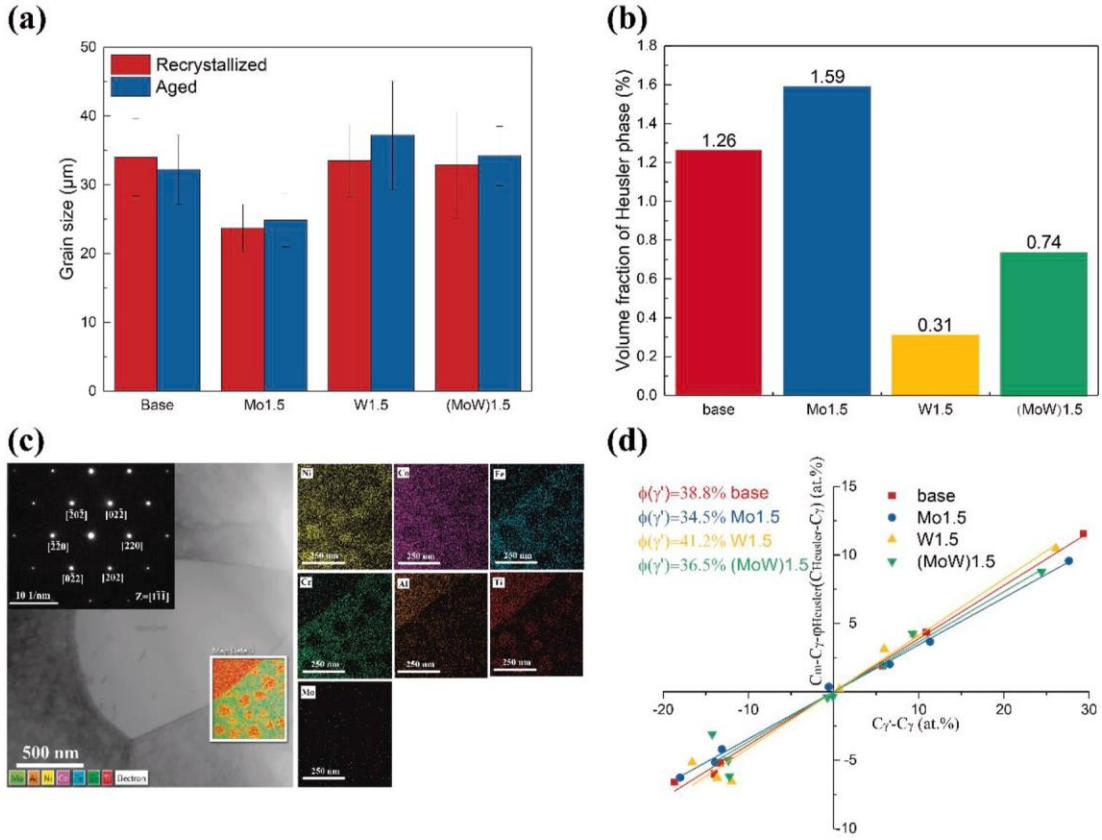
(a)
Recrystallized
Aged
Grain size (μm)
Base
Mo1.5
W1.5
(MoW)1.5
(b)
Volume fraction of Heusler phase (%)
1.26
1.59
0.31
0.74
base
Mo1.5
W1.5
(MoW)1.5
(c)
500 nm
(d)
ϕ(γ')=38.8% base
ϕ(γ')=34.5% Mo1.5
ϕ(γ')=41.2% W1.5
ϕ(γ')=36.5% (MoW)1.5
base
Mo1.5
W1.5
(MoW)1.5
Cγ'-Cγ (at.%)

Fig 6

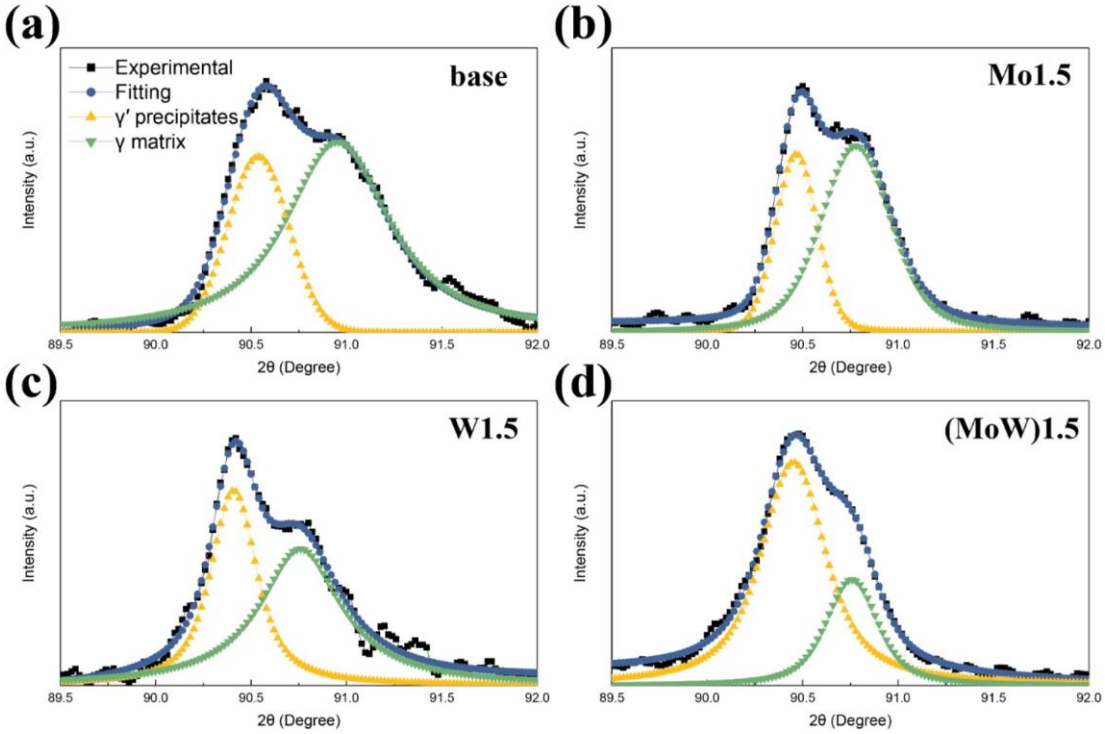
(a)
Experimental
Fitting
γ′ precipitates
γ matrix
base
Intensity (a.u.)
89.5
90.0
90.5
91.0
91.5
92.0
2θ (Degree)
(b)
Mo1.5
Intensity (a.u.)
89.5
90.0
90.5
91.0
91.5
92.0
2θ (Degree)
(c)
W1.5
Intensity (a.u.)
89.5
90.0
90.5
91.0
91.5
92.0
2θ (Degree)
(d)
(MoW)1.5
Intensity (a.u.)
89.5
90.0
90.5
91.0
91.5
92.0
2θ (Degree)

Fig 7

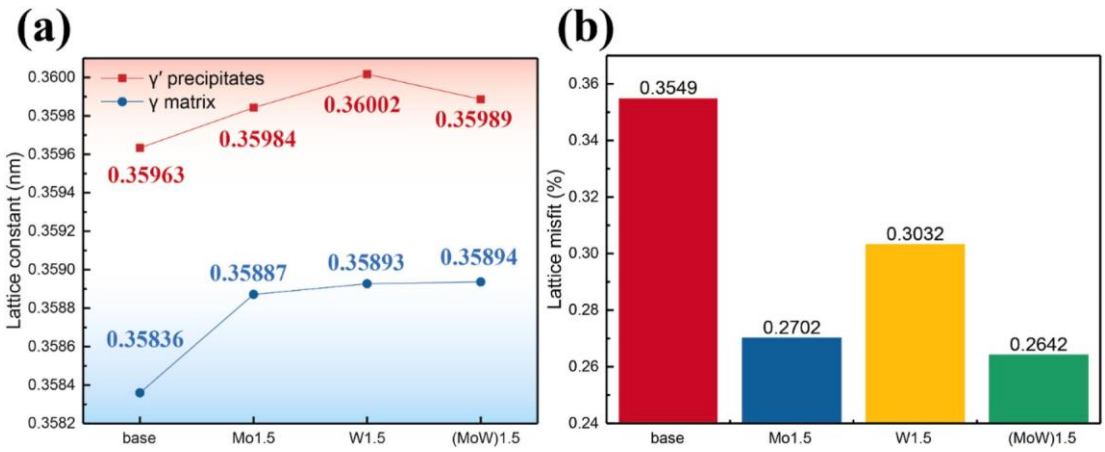
(a)
γ′ precipitates
γ matrix
Lattice constant (nm)
0.3600
0.3598
0.3596
0.3594
0.3592
0.3590
0.3588
0.3586
0.3584
0.3582
0.35963
0.35984
0.36002
0.35989
0.35836
0.35887
0.35893
0.35894
base
Mo1.5
W1.5
(MoW)1.5
(b)
Lattice misfit (%)
0.36
0.34
0.32
0.30
0.28
0.26
0.24
0.3549
0.2702
0.3032
0.2642
base
Mo1.5
W1.5
(MoW)1.5

Fig 8

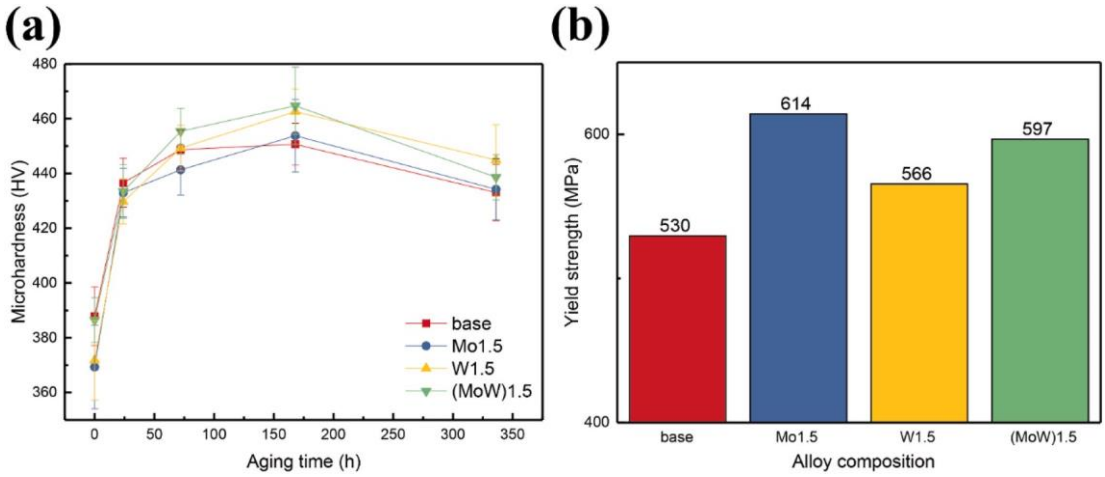
(a)
Microhardness (HV)
480
460
440
420
400
380
360
0
50
100
150
200
250
300
350
Aging time (h)
base
Mo1.5
W1.5
(MoW)1.5
(b)
Yield strength (MPa)
600
400
530
614
566
597
base
Mo1.5
W1.5
(MoW)1.5
Alloy composition

Fig 9

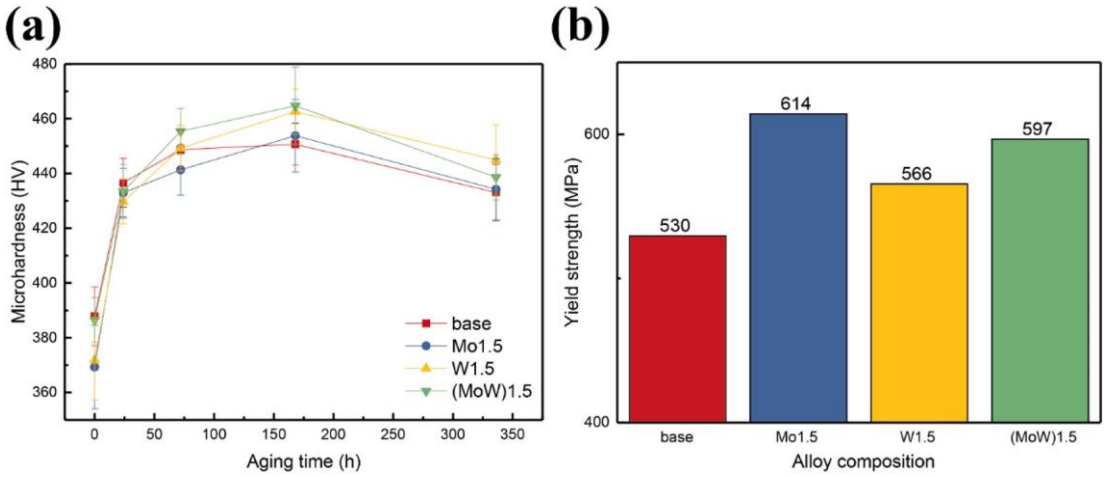
(a)
Microhardness (HV)
480
460
440
420
400
380
360
0
50
100
150
200
250
300
350
Aging time (h)
base
Mo1.5
W1.5
(MoW)1.5
(b)
Yield strength (MPa)
600
400
530
614
566
597
base
Mo1.5
W1.5
(MoW)1.5
Alloy composition

Fig 10

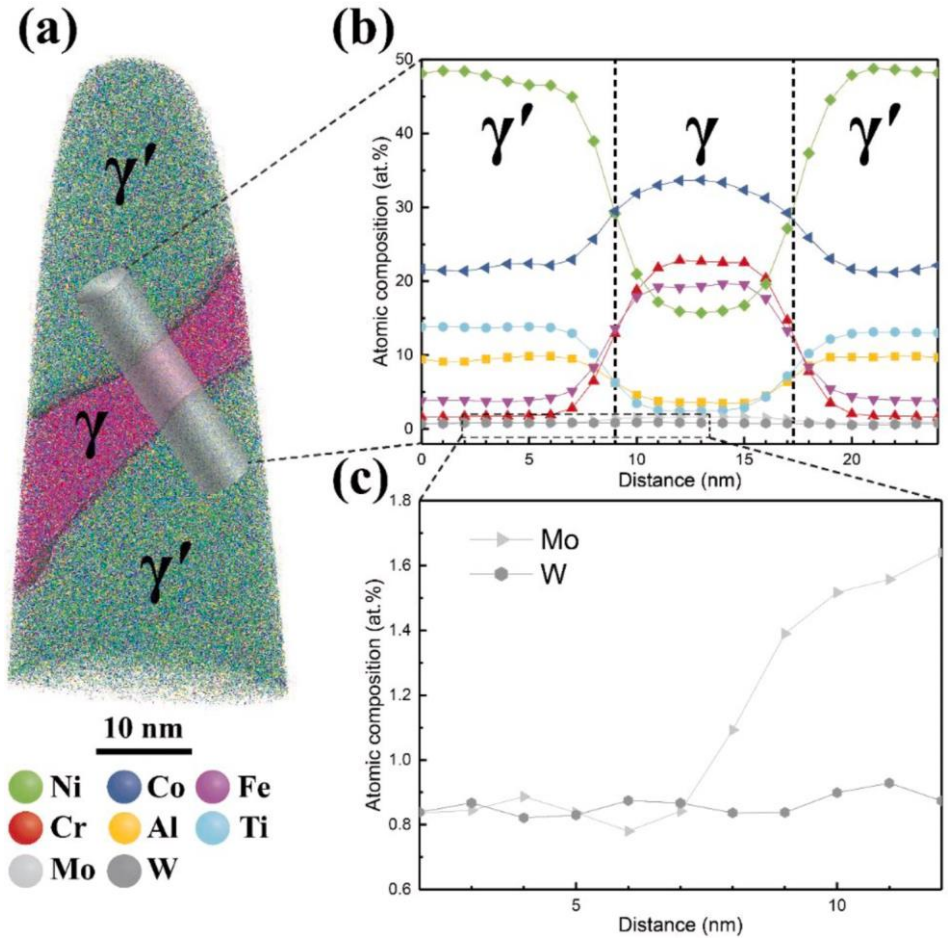
(a)
γ′
γ
γ′
10 nm
Ni
Co
Fe
Cr
Al
Ti
Mo
W
(b)
γ′
γ
γ′
Atomic composition (at.%)
Distance (nm)
(c)
Mo
W
Atomic composition (at.%)
Distance (nm)

Fig 11

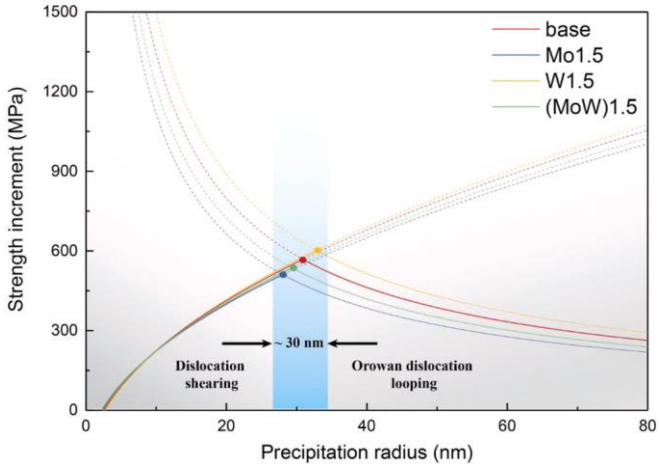
base
Mo1.5
W1.5
(MoW)1.5
Strength increment (MPa)
Precipitation radius (nm)
~ 30 nm
Dislocation shearing
Orowan dislocation looping
0
300
600
900
1200
1500
0
20
40
60
80